

# Gyrokinetic simulations of electrostatic microturbulence in ADITYA-U tokamak

Tajinder Singh<sup>1,\*</sup> , Deepti Sharma<sup>2</sup> , Tanmay Macwan<sup>2</sup> , Sarveshwar Sharma<sup>2,3,\*</sup> ,  
Joydeep Ghosh<sup>2,3</sup> , Abhijit Sen<sup>2,3</sup> , Zhihong Lin<sup>4</sup>  and Animesh Kuley<sup>1,\*</sup> 

<sup>1</sup> Department of Physics, Indian Institute of Science, Bangalore 560012, India

<sup>2</sup> Institute for Plasma Research, Bhat, Gandhinagar 382428, India

<sup>3</sup> Homi Bhabha National Institute, Anushaktinagar, Mumbai, Maharashtra 400094, India

<sup>4</sup> Department of Physics and Astronomy, University of California Irvine, Irvine, CA, 92697, United States of America

E-mail: [stajinder@iisc.ac.in](mailto:stajinder@iisc.ac.in), [sarvesh@ipr.res.in](mailto:sarvesh@ipr.res.in) and [akuley@iisc.ac.in](mailto:akuley@iisc.ac.in)

Received 28 March 2022, revised 19 February 2023

Accepted for publication 10 March 2023

Published 24 March 2023



## Abstract

Global gyrokinetic simulations of the electrostatic microturbulence driven by the pressure gradients of thermal ions and electrons are carried out for the ADITYA-U tokamak geometry using its experimental plasma profiles and with collisional effects. The dominant instability is trapped electron mode (TEM) based on the linear eigenmode structure and its propagation in the electron diamagnetic direction. Collisional effects suppress turbulence and transport to a certain extent. Zonal flow is not playing a critical role in the TEM saturation, which is dominated by the inverse cascade. The frequency spectrum of the electrostatic fluctuations is in broad agreement with the experimentally recorded spectrum in the ADITYA-U, with a bandwidth ranging from  $\sim 0$  to 50 kHz.

Keywords: simulation, gyrokinetic, tokamak, microturbulence

(Some figures may appear in colour only in the online journal)

## 1. Introduction

In fusion reactors [1, 2], the energy and particle confinement time must be long enough to achieve a net energy balance between the energy supplied to heat the system and the energy produced by the fusion process in the plasma. The energy and particle losses observed in magnetic fusion experiments are significantly higher than predicted values for the collisional processes [3]. This so-called anomalous transport is believed to be primarily due to small-scale instabilities called micro-instabilities caused by the temperature and density gradient of plasma species [4]. Therefore, understanding the physics of turbulent transport is of paramount importance in magnetically

confined plasma experiments. The design of future reactors relies on the extrapolation of the turbulent transport levels from current fusion experiments to much larger future experiments such as the International Thermonuclear Experimental Reactor (ITER) [5, 6].

Thanks to the spectacular advances in high-performance computing, it has become possible to carry out large-scale numerical simulations, using various plasma models, to study the characteristics of turbulence and transport. For example, simulation results using sophisticated gyrokinetic codes [7] have shown good agreement with experimental observations from tokamaks. An important objective of these simulations is to find a physical basis for the empirical scaling of the turbulent transport levels from first-principles, state-of-the-art numerical modeling [8–10]. Advanced gyrokinetic simulation codes enable an in-depth study of small-scale turbulence, such as that arising from drift waves, that is widely believed to be the cause of anomalous transport [4]. Various simulation codes treat the problem at different levels of complexity to capture some of the crucial physics features, related to the small-scale

\* Authors to whom any correspondence should be addressed.



Original Content from this work may be used under the terms of the [Creative Commons Attribution 4.0 licence](https://creativecommons.org/licenses/by/4.0/). Any further distribution of this work must maintain attribution to the author(s) and the title of the work, journal citation and DOI.

modes like the ion temperature gradient (ITG) and the trapped electron mode (TEM).

Based on the numerical methods used to solve the underlying equations, the gyrokinetic codes are classified into three categories: Lagrangian, Eulerian, and semi-Lagrangian. All these methods have their own advantages and disadvantages. The gyrokinetic codes such as gyrokinetic toroidal code (GTC) [11], ORB5 [12], GEM [13] are based on the Lagrangian approach that represents the plasma by a finite number of marker particles. To reduce the particle noise due to Monte Carlo sampling of phase space, these codes use the  $\delta f$  scheme [14]. The gyrokinetic codes GENE [15], GKV [16], GYRO [17] are based on the Eulerian approach. In this method, the time stationary phase space mesh is used for the discretization of the Vlasov equation. Whereas the semi-Lagrangian approach-based codes such as GYSELA [18] combine the benefits of both the Lagrangian and Eulerian approaches with a good phase space description and enhanced numerical stability.

Many gyrokinetic simulations of electrostatic microturbulence using realistic device geometry and experimental plasma profiles have found the signatures of ITG/TEM turbulence. For example, a comparison of the experimentally measured plasma fluctuations and turbulent transport is made against the local electrostatic gyrokinetic simulations of L-mode discharge of the DIII-D tokamak using the GS2 code [19], in which the ITG turbulence was investigated. The nonlinear electrostatic gyrokinetic simulations of L-mode discharge of DIII-D using the GYRO code show similar electron temperature and density fluctuations in the ITG/TEM unstable plasma, consistent with the experimental observations [20]. Similarly, a validation study of the gyrokinetic electrostatic simulations using GYRO code has been done for the ITG and TEM dominated L-mode plasmas of Alcator C-Mod tokamak [21].

Turbulence and transport in tokamaks can be greatly influenced by collisions and zonal flow. The zonal flow interaction with the turbulence has been extensively studied. For example, it is widely accepted that the zonal flow plays an essential role in regulating the ITG turbulent transport [11, 22]. However, in contrast to the ITG turbulence, the effect of zonal flow on the TEM turbulent transport is found to depend on the parameters such as the electron to ion temperature ratio, magnetic shear, the electron temperature gradient scale length, and the ratio of electron temperature gradient to density gradient [13, 23–26]. The collisions can effect the turbulence and transport directly by affecting the linear microturbulence drive or indirectly by affecting the coherent phase space structure. It has been found that the collisional effects can reduce the ITG turbulence growth rate, can lead to the stabilization of TEM turbulence, or can lead to a transition from TEM to ITG turbulence by the de-trapping of electrons [26–28]. The recent gyrokinetic simulations using GTC have shown the effects of collisions on the ITG and TEM dominant discharges of the DIII-D tokamak [29].

GTC has been applied to several different geometries, for example, tokamaks [11] and field-reversed configuration [30] to study turbulent transport. Recently, GTC was upgraded to simulate turbulence in the 3D devices called stellarators

[31–33]. In the present work, we have used GTC to study the microturbulence in the ADITYA-U tokamak. ADITYA-U is a medium-sized, air-core tokamak, that has recently been upgraded from the ADITYA tokamak [34–37] to incorporate a new set of divertor coils for shaped plasma operations with a new vacuum vessel along with a new toroidal belt limiter. Since its commissioning, several experiments relevant to the operation of future fusion devices such as ITER have been performed [35–37], including experiments on generation, transport and control of runaway electrons [36, 37], plasma disruption [36, 37], transient transport phenomena such as cold-pulse propagation [37, 38] and plasma detachment [37]. However, there are very few simulation studies on the ADITYA-U tokamak.

In the present work, self-consistent gyrokinetic simulations have been carried out using GTC to investigate the role of electrostatic microturbulence, such as ITG and TEM, in driving the turbulent transport in the circular plasmas (limiter plasmas) of the ADITYA-U tokamak. The ion diffusivity and electron heat conductivity values estimated from the experiments are in fair agreement with the values obtained from the simulations. The turbulent fluxes are found to be driven by the TEM in ADITYA-U. The simulated frequency spectra of electrostatic fluctuations match well with those measured using Langmuir probes in the edge region of the plasma. The simulations with and without collisions show that the collisional effects suppress the turbulence and transport to a certain extent. The nonlinear simulations show that the zonal flow is not playing a crucial role in the nonlinear saturation, which is dominated by the inverse cascade of the higher toroidal mode numbers to the lower ones. These simulation findings could be helpful in setting up future experiments in the ADITYA-U tokamak. The present work is the first ever simulation study to understand the turbulence and transport in ADITYA-U. As a first step, we have restricted ourselves only to electrostatic simulations. Electromagnetic effects could have an impact on turbulence and transport [39] and will be investigated in a future study.

The rest of the paper is presented as follows: the geometry, equilibrium quantities, and experimental results for the ADITYA-U tokamak discharge shot # 33536 are discussed in section 2. In section 3, the simulation and physics model used are presented. In section 4, linear and nonlinear simulations of the microturbulence are discussed. In section 5, the conclusions have been made.

## 2. ADITYA-U Experiment

ADITYA-U is a medium-sized tokamak with a major radius of 0.75 m and a minor radius of 0.25 m [34–37]. For the present simulation, a hydrogen (main ion) plasma discharge (shot # 33536) has been used, in which the plasma is operated in the limiter configuration. The plasma parameters of the discharge are plasma current  $\sim 150$  kA, central chord-averaged density  $\sim 2.3 \times 10^{19} \text{ m}^{-3}$ , central chord-averaged electron temperature  $\sim 250$  eV and ion temperature  $\sim 80$  eV. The radial profile of plasma density has been obtained from a multi-channel microwave interferometer [38, 40]. The

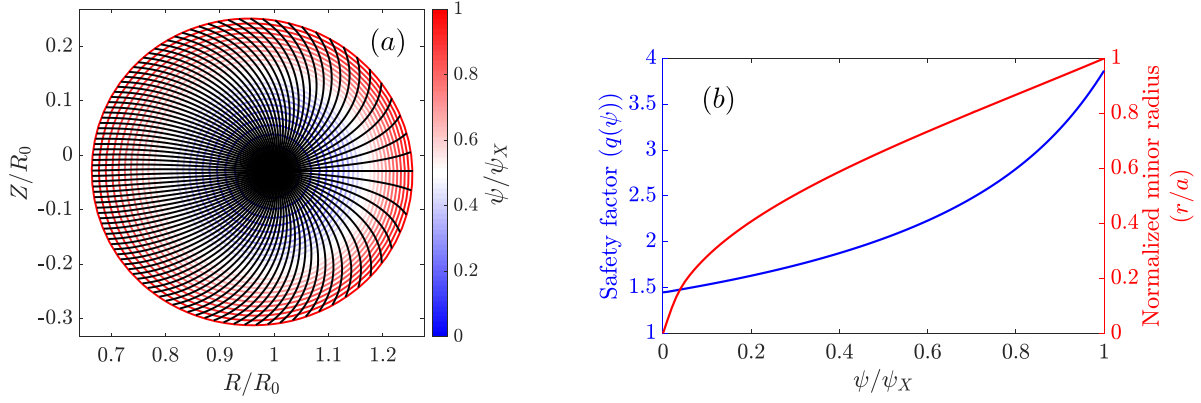


**Figure 1.** Equilibrium mesh on the poloidal plane (a). The contours show the poloidal flux normalized to the value at the last closed flux surface  $\psi_X$  and the black lines are the curves of constant poloidal angle and the safety factor (blue curve) and normalized minor radius (red curve) as a function of the normalized poloidal flux (b) for ADITYA-U discharge shot # 33536.

radial profile of electron temperature is reconstructed using multi-chord soft x-ray emission intensity measurements in the core plasma region, and the Langmuir probe (single/triple) is used for the spectral analysis of edge temperatures [38]. The core ion temperature is measured using spectroscopic diagnostics [41]. The radial profile of ion temperature is assumed to be the same as the plasma pressure profile. Figure 1(a) shows the equilibrium mesh on the poloidal plane for discharge shot # 33536 obtained with IPREQ code [42]. The black lines in the figure represent the curves of a constant poloidal angle, while the contours represent the poloidal flux normalized with the value at the last closed flux surface (LCFS),  $\psi_X$ . The on-axis magnetic field  $B_0$  is 1.44 T, the distance at the magnetic axis  $R_0$  is 0.7641 m. Figure 1(b) shows the safety factor profile obtained from the equilibrium simulations carried out using IPREQ code [42] and the normalized minor radius as a function of normalized poloidal flux. The equilibrium quantities for the ADITYA-U discharge are written in cylindrical coordinates that are transformed to magnetic Boozer coordinates to be used as input to GTC. The edge region (region near to the LCFS) of the ADITYA-U tokamak is thoroughly diagnosed by several sets of Langmuir probes [38]. A broadband fluctuation spectrum is observed in the frequency range of  $\sim 0$ –50 kHz in the measured density fluctuations sampled at 100 kHz. The rack-Langmuir probes [38] are also used for measurements of the radial profile of density in the edge regions. The density fluctuations are measured using both single and triple Langmuir probes in ADITYA-U. The density in the edge region in the present study is measured from the ion-saturation current drawn by the probe. Density fluctuations are generally large in magnitude in comparison to the temperature fluctuations and hence the temperature fluctuations are ignored in the density fluctuations estimation [43]. Ion-saturation current measurements represent the density fluctuations quite well, especially close to the LCFS  $\psi_X$  of the tokamak [44]. The variation in the magnitude and frequency of density fluctuations from shot-to-shot measurements in the set of represented discharges of ADITYA-U remains within 10%. For the simulations, the mean density and temperature profiles are used. The various ADITYA-U parameters and plasma

**Table 1.** ADITYA-U tokamak and plasma parameters for a typical experimental discharge.

Minor radius	0.25 m
Major radius	0.75 m
On-axis magnetic field	1.44 T
On-axis electron temperature	250 eV
On-axis ion temperature	80 eV
On-axis electron density	$2.3 \times 10^{19} \text{ m}^{-3}$
Energy confinement time	$\sim 10$ ms
Ion acoustic speed	$1.55 \times 10^5 \text{ m s}^{-1}$
Ion gyro-radius	$6.34 \times 10^{-4} \text{ m}$
Electron gyro-radius	$2.61 \times 10^{-5} \text{ m}$
Ion thermal velocity	$8.76 \times 10^4 \text{ m s}^{-1}$
Electron thermal velocity	$6.63 \times 10^6 \text{ m s}^{-1}$

parameters are shown in table 1 for a typical experimental discharge.

### 3. Simulation and physics model

GTC uses the field-aligned coordinate system to study the magnetically confined plasma with nested flux surfaces [10] which is suitable for the efficient integration of particle trajectories that move primarily along the magnetic field lines. The fully kinetic dynamics of the plasma particles requires a smaller step size to resolve the cyclotron motion which in turn makes the simulations computationally expensive. To resolve this issue, a coordinate transformation is made from particle coordinates to the guiding-center coordinates. This transformation reduces the dimensionality of the system from 6D to 5D due to the averaging of the gyro-phase of the charged particles along the magnetic field lines [45, 46]. By doing so, the high-frequency cyclotron motion gets eliminated from the particle trajectory [47]. So, the resulting gyrokinetic equations involve the motion of the plasma particles in the reduced 5D space. The gyrokinetic equations describing the toroidal plasma in the inhomogeneous magnetic field in the five-dimensional space  $(\vec{X}, v_{\parallel}, \mu)$  is given by

$$\left( \partial_t + \vec{X} \cdot \nabla + v_{\parallel} \partial_{v_{\parallel}} \right) f_i(\vec{X}, \mu, v_{\parallel}, t) = C_i f_i, \quad (1)$$

$$\dot{\vec{X}} = \frac{\vec{B}^*}{B_{\parallel}^*} v_{\parallel} + \vec{v}_E + \vec{v}_c + \vec{v}_g, \quad (2)$$

$$\dot{v}_{\parallel} = -\frac{1}{m_i} \frac{\vec{B}^*}{B_{\parallel}^*} \cdot (\mu \nabla B + Z_i \nabla \phi), \quad (3)$$

where  $\vec{B}^* = \vec{B} + B v_{\parallel} / \Omega_i (\nabla \times \hat{b})$ ,  $B_{\parallel}^* = \hat{b} \cdot \vec{B}^*$ ,  $C_i$  is the pitch-angle collision operator described in [48],  $\vec{v}_E$  is the  $\vec{E} \times \vec{B}$  drift velocity, and  $\vec{v}_c$ , and  $\vec{v}_g$  are magnetic drift velocities due to the curvature and gradient in magnetic field, that are given by

$$\vec{v}_E = \frac{c \hat{b} \times \nabla \phi}{B_{\parallel}^*}, \quad (4)$$

$$\vec{v}_c = \frac{B}{B_{\parallel}^*} \frac{v_{\parallel}^2}{\Omega_i} \nabla \times \hat{b}, \quad (5)$$

$$\vec{v}_g = \frac{\mu}{m_i \Omega_i} \frac{\vec{B} \times \nabla B}{B_{\parallel}^*} \quad (6)$$

where  $B$  is the amplitude of equilibrium magnetic field at particle position,  $B^*$  is the equilibrium magnetic field amplitude at the guiding-center position of the particle,  $Z_i$  is the charge,  $m_i$  is the mass, and  $\Omega_i$  is the cyclotron frequency of the ion. To reduce the particle noise due to Monte Carlo sampling of the phase space,  $\delta f$  method [14] is used in which only the perturbed part of the particle distribution is evolved with time. The distribution function is written as the sum of equilibrium and perturbed parts,  $f_i = f_{0i} + \delta f_i$ , with the equilibrium part satisfying the 5D-gyrokinetic equation. Further, an additional dynamical variable, particle weight, is defined as  $w_i = \delta f_i / f_i$ , that satisfies the following equation

$$\frac{dw_i}{dt} = (1 - w_i) \left[ -\vec{v}_E \cdot \frac{\nabla f_{0i}}{f_{0i}} + \frac{Z_i}{m_i} \frac{\vec{B}^*}{B} \cdot \nabla \phi \frac{1}{f_{0i}} \frac{\partial f_{0i}}{\partial v_{\parallel}} \right]. \quad (7)$$

The electrostatic potential  $\phi$  appearing in equations of motion and weight equation is decomposed into a zonal component averaged over the flux surface and a fluctuating part  $\phi = \langle \phi \rangle + \delta \phi$  with  $\langle \delta \phi \rangle = 0$ , where  $\langle \dots \rangle$  represents the flux-surface averaging. To study the effect of electrons on turbulent transport and to include the instabilities like TEM in the simulations, the kinetic treatment of electrons is required. The kinetic treatment of electrons in the gyrokinetic framework requires a smaller time step due to fast parallel motion, thus increasing the simulation cost. To overcome this limitation, the fluid-kinetic hybrid model is implemented in GTC [49]. To solve the drift kinetic equation for electron, the electron response and electrostatic potential are expanded in the smallness parameter  $\delta$ , where  $\delta$  is the ratio of drift wave frequency to the electron transit frequency; as  $f_e = f_{0e} + \frac{e \delta \phi^{(0)}}{T_e} f_{0e} + \delta g_e$ , and  $\delta \phi = \delta \phi^{(0)} + \delta \phi^{(1)}$ . The nonadiabatic parts  $\delta g_e$ ,  $\delta \phi^{(1)}$  are smaller than the adiabatic parts by a factor of  $\delta$ . The electrostatic potential is acquired from Poisson's equation in a spatial network of grids after the charge density is accumulated on the grids. However, in the gyrokinetic framework,

gyrokinetic transformation needs to be incorporated in Poisson's equation as well. This results in a gyrokinetic version of Poisson's equation involving the electrostatic potential and particle density that are averaged over the charge ring with a radius of local gyro-radius of the charged particle. Numerically, this gyro-ring is represented by fewer points (4, 8, 16, etc). The electrostatic potential in the lowest order is acquired from the gyrokinetic Poisson equation given below

$$\frac{(\tau + 1)e \delta \phi^{(0)}}{T_e} - \frac{\tau e \delta \tilde{\phi}^{(0)}}{T_e} = \frac{\delta \bar{n}_i - \langle \delta \bar{n}_i \rangle}{n_0}, \quad (8)$$

where  $\tau = T_e / T_i$ ,  $n_0$  is the equilibrium electron density,  $\delta \tilde{\phi}^{(0)}$  is the second gyro-averaged perturbed potential defined as

$$\delta \tilde{\phi}^{(0)}(\vec{x}) = \frac{1}{2\pi} \int d^3 \vec{v} \int d^3 \vec{X} f_0(\vec{X}) \delta \bar{\phi}^{(0)}(\vec{X}) \delta(\vec{X} + \vec{\rho} - \vec{x}),$$

with  $\vec{x}$  and  $\vec{X}$  represents the coordinates of particle position and the particle guiding center position respectively and  $\vec{\rho}$  is gyro-radius vector.  $\delta \bar{\phi}^{(0)}$  is the first gyro-averaged perturbed potential defined by

$$\delta \bar{\phi}^{(0)}(\vec{X}) = \int d^3 \vec{x} \int \frac{d\alpha}{2\pi} \delta \phi^{(0)}(\vec{x}) \delta(\vec{x} - \vec{X} - \vec{\rho}),$$

and similarly

$$\delta \bar{n}_i(\vec{x}) = \int d^3 \vec{X} \int \frac{d\alpha}{2\pi} \delta f(\vec{X}) \delta(\vec{x} - \vec{X} - \vec{\rho}),$$

is the ion perturbed density at the guiding-center,  $\alpha$  is the gyro-phase. The second gyro-averaged perturbed electrostatic potential ( $\delta \tilde{\phi}^{(0)}$ ) is calculated using Padé approximation [50]. In the higher order, the electron dynamics is governed by the drift kinetic equation in  $\delta g_e$ . To resolve the electron dynamics, in a single push step for ion, electron is pushed several times, known as the subcyclotron ratio. An iterative time stepping sequence has been used to update the particle guiding center orbits and field quantities. At  $i$ th time step all the field quantities are computed and at  $(i+1)$ th time step ion orbits are pushed using the ion gyrokinetic equation. The electron weight  $w_e = \delta g_e / f_e$  are evolved according to the equation

$$\frac{dw_e}{dt} = \left( 1 - \frac{e \delta \phi^{(0)}}{T_e} - w_e \right) \left[ -\vec{v}_E \cdot \nabla \ln f_{0e} |_{v_{\perp}} - \frac{\partial}{\partial t} \left( \frac{e \delta \phi^{(0)}}{T_e} \right) - (\vec{v}_d + \delta \vec{v}_E) \cdot \nabla \left( \frac{e \phi}{T_e} \right) \right] \quad (9)$$

where  $\delta \vec{v}_E = (c/B^*) \hat{b} \times \nabla \delta \phi$ , the notation ' $|_{v_{\perp}}$ ' indicates that the gradient operator on ' $\ln f_{0e}$ ' is performed with  $v_{\perp}$  held fixed. The electron orbits are pushed from  $i$ th time step to  $(i+1)$ th time step using all the field quantities at  $i$ th time step in equation (9). The non-zonal electrostatic perturbed potential till the first order correction is related to the density perturbation as

$$e \delta \phi / T_e = e \delta \phi^{(0)} / T_e - \frac{\delta n_e - \langle \delta n_e \rangle}{n_0}, \quad (10)$$

with  $\delta n_e = \int \delta h_e d^3\vec{v}$ . Equations (9) and (10) can be solved repeatedly to reach the higher order in the expansion. The convergence test shows that the second order expansion is sufficient for the present study. The equations for ions are solved only once. Finally, all the particle orbits and non-zonal components of field quantities are updated at  $(i + 1)$ th time step and the zonal component of the electrostatic potential at  $(i + 1)$ th time step is obtained by solving

$$\frac{\tau e \left( \langle \phi \rangle - \langle \tilde{\phi} \rangle \right)}{T_e} = \frac{\langle \delta \bar{n}_i \rangle - \langle \delta n_e \rangle}{n_0}. \quad (11)$$

The flux-surface-averaged gyrokinetic Poisson equation representing zonal component is solved by traditional integration, while a finite difference-based gyrokinetic Poisson solver is incorporated in GTC for the non-zonal component using HYPRE library [51] to solve the resulting matrix equation. The electrostatic field is then scattered back to the guiding-center position to update the orbit. The out-of-boundary particles are brought back to the simulation domain by the energy-conserving boundary conditions. Fixed boundary conditions are applied for all fluctuating quantities at both sides of radial simulation domain.

Fokker–Planck collision operator for the collisions between like species and Lorentz pitch angle scattering operator for the collisions between unlike species, are implemented where the momentum and energy conservation are enforced on the neoclassical mesh [48]. The dimensionless effective collision frequency defined in GTC is  $\nu^* = \epsilon^{-3/2} \nu q R_0 / v_{th}$ , with  $\epsilon = r/R_0$  as the local inverse aspect-ratio,  $r$  is the radius evaluated on the outer mid-plane,  $\nu$  is the physical collision frequency, and  $v_{th} = \sqrt{T_{0\alpha}/m_\alpha}$  is the thermal velocity of the plasma species  $\alpha$ .

#### 4. Microturbulence simulations

This section presents the electrostatic gyrokinetic simulations of the low-frequency drift wave instabilities driven by the gradient in the plasma density and temperature, performed using GTC. Figure 2 shows the plasma profile (figure 2(a)) and the corresponding normalized gradient  $R_0/L_X$  (figure 2(b)) used in simulations, where  $L_X$  is the profile gradient scale length given by  $1/L_X = -\partial(\ln X)/\partial r$ ,  $r$  is the local minor radius. The gradient in the plasma profile is steep at the LCFS, which can drive electrostatic instabilities such as ITG instability, TEM instability. The simulation domain is from  $\psi_{inner} = 0.1\psi_X$  to  $\psi_{outer} = 1.0\psi_X$ , where the poloidal flux  $\psi$  values are normalized to the value at the LCFS  $\psi_X$ . The ion species is the proton, and their dynamics is described by the gyrokinetic equations, and the electrons are treated kinetically, according to the fluid-kinetic hybrid model, as described in section 2. Both the passing and trapped electrons have been included in the simulations. The proton to electron mass ratio is  $m_p/m_e = 1836$ . GTC uses three meshes: equilibrium mesh, as shown in figure 1(a), turbulence mesh, and neoclassical mesh. For the simulations, 200 radial grid points, 3000 poloidal grid points, and 32 grid points in the parallel direction

are used for the turbulence mesh. The microturbulences under investigation are ITG and TEM that satisfy  $k_{\parallel} \ll k_{\perp}$ , thus the turbulence mesh requires fewer grid points in the parallel direction as compared to the radial and poloidal grid points. The radial, poloidal, and toroidal grid numbers used for the neoclassical mesh are 64, 64, and 32, respectively, based on the convergence studies. First, the time step convergence is done, followed by the convergence of electron subcycles, and finally, the convergence for particle number is done. The time step size used is  $0.025R_0/C_s$ , where  $C_s/R_0$  is  $2.0258 \times 10^5 \text{ s}^{-1}$  and  $C_s = \sqrt{T_e/m_i}$  is the ion-acoustic wave speed. The plasma is represented by the marker particles that are loaded uniformly throughout the simulation domain. From the convergence test, 50 marker particles per cell are used, and the number of electron subcycles is 2. The system size in this work is set as  $a = 175\rho_i$ , where  $\rho_i$  is the ion gyro-radius.

The effective charge number  $Z_{eff}$  is taken as 1.0 while considering the collisions in the simulations. The on-axis effective collision frequency  $\nu^*$  is 0.04 for electrons and 0.26 for ions. The turbulent transport and the zonal flow physics are the universal aspects of the drift wave instabilities [4, 10]. To study the effect of zonal flow on turbulent transport, an additional nonlinear simulation is run by artificially suppressing the zonal flow during the simulation. Figure 3 shows the poloidal cross-sections of the electrostatic potential at different simulation times for the two nonlinear simulations. Figure 3(a) shows the contour plot of the electrostatic potential in the linear phase of the simulation at time  $t = 3.5R_0/C_s$ . The linear eigenmode structure that peaks near the flux surface with  $\psi \sim \psi_X$  looks like a typical ballooning mode which is localized on the outer mid-plane side where the curvature is bad in the region of steep profile gradient with the eddies elongated along the direction of the profile gradient. Figure 3(b) shows the enlarged view of the mode structure on the poloidal plane. The mode propagates in the electron diamagnetic direction, indicating that the TEM turbulence is unstable, which is also consistent with the earlier gyrokinetic simulations of the DIII-D pedestal with steep profile gradients using GTC [52]. These findings are similar to the earlier investigations made for the reversed field pinch [53], tokamak [54–59] and stellarator [60, 61] plasmas in the region of steep plasma profile gradients. Figures 3(c) and (d) show the contour plot of the electrostatic potential in the nonlinear phase of the simulation at time  $t = 9.5R_0/C_s$  with zonal flow (figure 3(c)) and without zonal flow (figure 3(d)). In the nonlinear phase, the coupling between various toroidal modes and the interaction with the self-generated zonal flow leads to the turbulence spreading from the edge to the core of the tokamak. It illustrates that the global effects play an important role in linking the turbulent transport from the edge to the core of the tokamak.

The radial-time variation of the root-mean-squared electrostatic potential has been shown in figure 4. Figure 4(a) shows the radial variation of root-mean-squared electrostatic potential at three different times  $t = 3R_0/C_s$  (blue),  $9R_0/C_s$  (red) and  $15R_0/C_s$  (black). It is clear that in the nonlinear stage, turbulence structures spread far away from the location of the linear eigenmode. The turbulence spreading takes place in

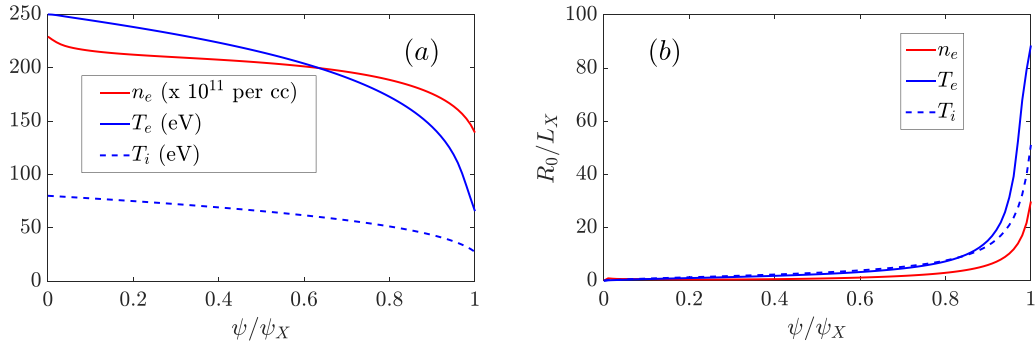


**Figure 2.** The profiles (a) and the corresponding normalized gradient (b) being used for the microturbulence simulations of ADITYA-U discharge shot # 33536.

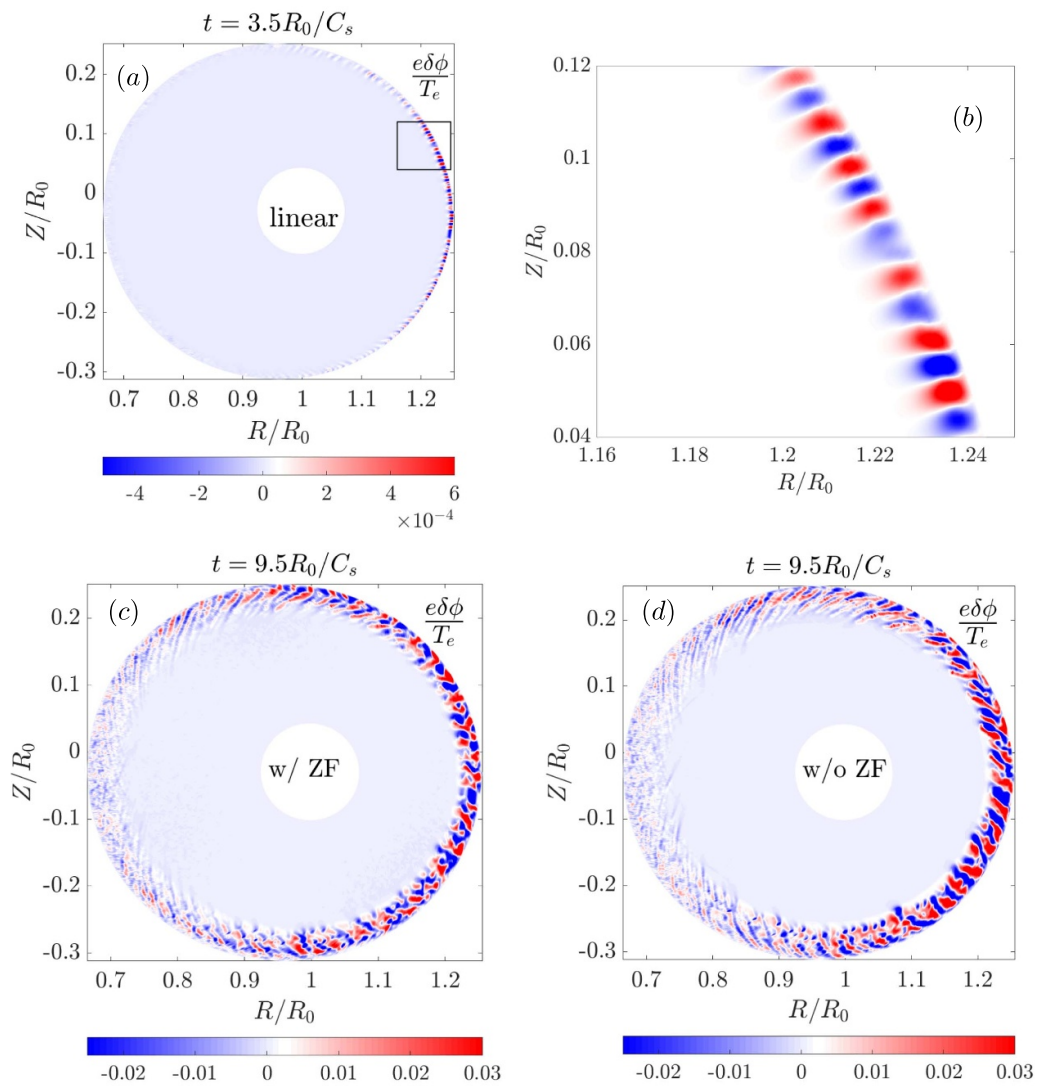


**Figure 3.** The electrostatic perturbed potential on the poloidal plane in the linear phase at time  $t = 3.5R_0/C_s$  (a), and the enlarged view of the linear eigenmode structure (b). The electrostatic potential in the nonlinear phase at time  $t = 9.5R_0/C_s$  with zonal flow (c), and without zonal flow (d).

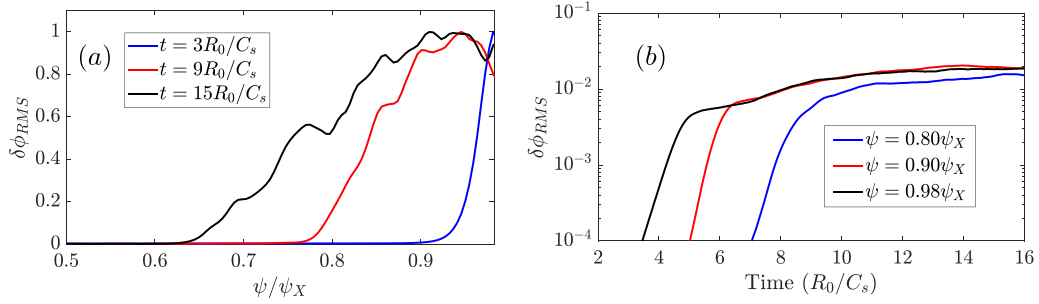


**Figure 4.** (a) The radial variation of the root-mean-squared electrostatic perturbed potential normalized to the maximum value at three different times  $3R_0/C_s$  (blue),  $9R_0/C_s$  (red) and  $15R_0/C_s$  (black), and (b) the time history of the root-mean-squared perturbed electrostatic potential in the region of turbulence spreading at three different flux surfaces with  $0.80\psi_X$  (blue),  $0.90\psi_X$  (red), and  $0.98\psi_X$  (black).

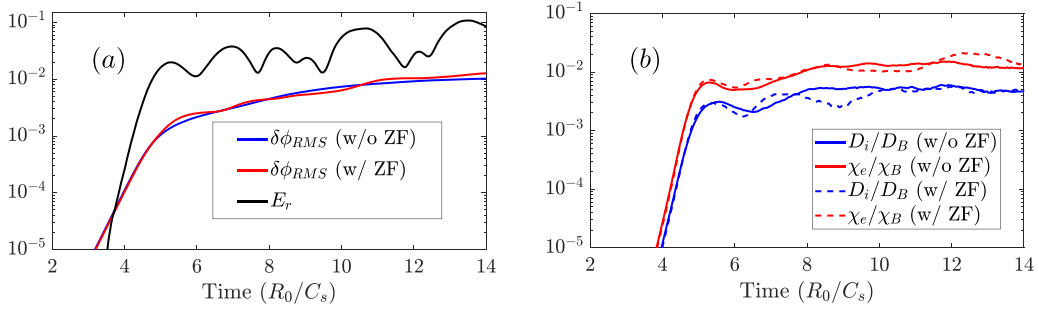


**Figure 5.** (a) The time history of the root-mean-squared electrostatic perturbed potential without zonal flow (blue), with zonal flow (red) and the radial electric field resulting from the turbulence (black) at  $\psi \sim \psi_X$ . The root-mean-squared electrostatic potential is normalized by  $T_e/e$ , and the radial electric field is normalized by  $\sqrt{T_e/e}$ . (b) The time history of the ion diffusivity (blue) and electron heat conductivity (red) in the Bohm units, with (dashed) and without (solid) zonal flow at  $\psi \sim \psi_X$ .

the radial range  $\psi \in [0.68, 1.0]\psi_X$  over the simulation time. Figure 4(b) shows the time history of the root-mean-squared electrostatic potential in the region of turbulence spreading at three different flux surfaces with  $\psi = 0.80\psi_X$  (blue),  $0.90\psi_X$  (red), and  $0.98\psi_X$  (black). Thus, in the region of turbulence spreading TEM turbulence is unstable.

The role of zonal flow in regulating the turbulence and transport is shown in figure 5. Figure 5(a) shows the time history of root-mean-squared electrostatic potential without zonal flow (blue), with zonal flow (red) and the radial electric field resulting from the turbulence (black) at the flux surface with  $\psi = 0.98\psi_X$ . The blue and red lines are almost overlapping with each other, which shows that the zonal flow is not playing an important role in suppressing the turbulence. Furthermore, as shown in figure 5(b), the time histories of the ion diffusivity (blue) and electron heat conductivity (red) show similar saturation levels with zonal flow (dashed) and without the zonal flow (solid). So, the zonal flow does not have any effect on the transport as well. The nonlinear saturation is dominated by the inverse cascade of the higher toroidal and poloidal modes to the lower one, which is also clear from the comparison of figures 3(c) and (d), as there is not much difference in the turbulence structure. These results are supported by the earlier findings by the local simulations, stating that the zonal flow has an important contribution to the turbulent transport driven by TEM instability only when  $\eta_e = \nabla \ln T_e / \nabla \ln n_e \lesssim 1$  [23] and

for the current discharge of ADITYA-U,  $\eta_e \sim 4.0$  at  $\psi \sim \psi_X$ . Yet another global simulation study using GTC has shown that the zonal flow can play a crucial role in the case with  $T_e = T_i$  [24], while in ADITYA-U the electron temperature is about three times the ion temperature. Similarly, the flux-tube (local) simulations using GENE have shown that the zonal flow has little effect on the TEM turbulence saturation for the cases with strong electron temperature gradient and  $T_e = 3T_i$  [25], which is the case for ADITYA-U.

The dominant eigenmode is  $n=73$ ,  $m=271$  with the growth rate of  $\gamma = 2.98C_s/R_0$  and the real frequency of  $\omega = 2.79C_s/R_0$ . The wavenumber corresponding to the dominant mode is  $k_\perp \rho_i \sim 0.7$ . The simulations show that the collisions reduce the linear growth rate of the dominant mode by almost 9% and suppress the electrostatic fluctuations by almost 36%. The comparison of the root-mean-squared electrostatic potential without and with collisions is made in figure 6. Furthermore, the collisional effects reduce the ion heat conductivity by half, the ion diffusivity by more than half, the electron heat conductivity by  $\sim 7\%$ , and the electron diffusivity by half. The effect of collisions on various quantities have been shown in table 2. The root-mean-squared electrostatic potential and transport coefficients are averaged over times  $t \in [10, 15]R_0/C_s$ . Usually, the collisions have a stabilization effect on the TEM turbulence [28], but due to the smaller collision frequency for the trapped electrons

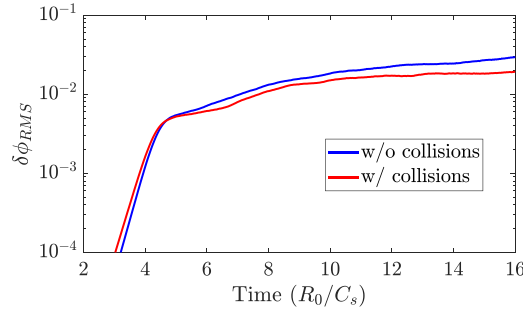


**Figure 6.** The time history of the root-mean-squared electrostatic potential without collisions (blue) and with collisions (red) at  $\psi = 0.98\psi_X$ .

**Table 2.** The effect of collisions on the turbulence growth rate  $\gamma$  in units of  $C_s/R_0$ , the root-mean-squared electrostatic potential  $\delta\phi_{RMS}$  in units of  $T_e/e$  and the transport coefficients  $D_\alpha$ ,  $\chi_\alpha$  ( $\alpha = i, e$ ) in units of  $m^2 s^{-1}$ .

	With collisions	Without collisions
$\gamma$	2.98	3.24
$\delta\phi_{RMS}$	0.0169	0.0229
$D_i$	0.25	0.67
$D_e$	0.32	0.64
$\chi_i$	0.89	1.80
$\chi_e$	1.20	1.28

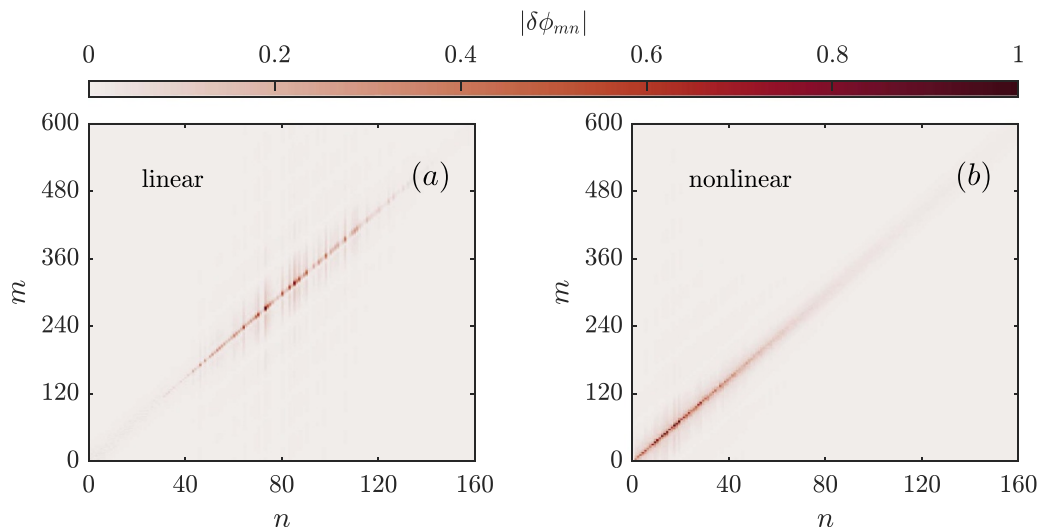


**Figure 7.** The 2D spectrum of the electrostatic potential on the flux surface  $\psi = 0.98\psi_X$  in the linear phase at time  $t = 3.5R_0/C_s$  (a) and in the nonlinear phase averaged over times  $t \in [10, 15]R_0/C_s$  (b).

TEM remains unstable even in the presence of collisions. The TEM turbulence and transport suppression (to some extent) caused by the collisional effects are due to the de-trapping of electrons.

Figure 7 shows the 2D spectrum ( $|\delta\phi_{mn}|$ ) of the electrostatic perturbed potential on the flux surface with  $\psi = 0.98\psi_X$  in the linear phase at time  $t = 3.5R_0/C_s$  (figure 7(a)) and in the nonlinear phase averaged over times  $t \in [10, 15]R_0/C_s$  (figure 7(b)). Because of the ballooning feature of the microturbulence and the extension of the potential in the direction parallel to the magnetic field while confining in

the perpendicular direction, the spectrum peaks on the mode rational surface (along the  $m = nq$  line) in the spectral domain. On the diagnosed flux surface  $\psi = 0.98\psi_X$ , the value of safety factor is  $q = 3.71$ . The spectrum in the linear phase is wide with a range  $n \in [40, 125]$ ,  $m \in [160, 460]$  with the most dominant mode at  $n = 73$ ,  $m = 271$ . The nonlinear coupling of the turbulent modes leads to the inverse cascade of the linearly unstable modes from high to low poloidal and toroidal modes. The spectrum in the nonlinear phase is averaged over the times  $t \in [10, 15]R_0/C_s$  that has a range  $n \in [0, 50]$ ,  $m \in [0, 190]$ .



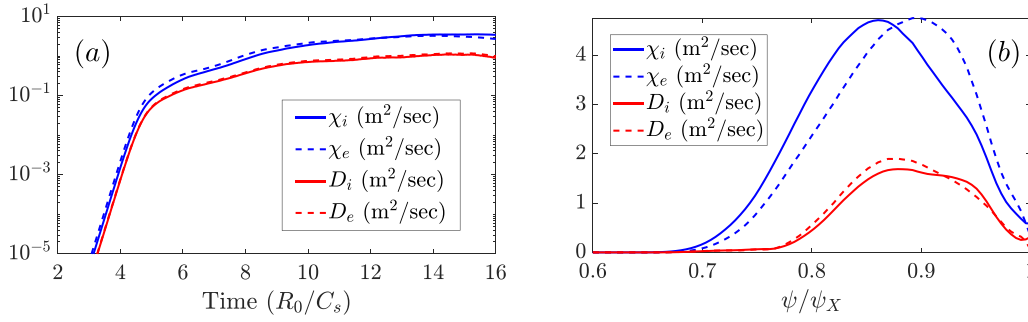


**Figure 8.** The time history (a) and radial variation (b) of the transport coefficients for ions and electrons.

The transport coefficients are calculated in GTC as

$$\chi_\alpha = \frac{1}{\langle |\nabla\psi|^2 \rangle n_{0\alpha} \frac{\partial T_{0\alpha}}{\partial \psi}} \left\langle \int d^3v \delta f_\alpha \left( \frac{1}{2} m_\alpha v^2 - \frac{3}{2} T_{0\alpha} \right) \vec{v}_E \cdot \nabla \psi \right\rangle$$

and

$$D_\alpha = \frac{1}{\langle |\nabla\psi|^2 \rangle \frac{\partial n_{0\alpha}}{\partial \psi}} \left\langle \int d^3v \delta f_\alpha \vec{v}_E \cdot \nabla \psi \right\rangle$$

where the angle bracket  $\langle \dots \rangle$  represents the flux-surface average and  $|\dots|$  represents the amplitude of the vector. GTC gives the diffusivity ( $D_\alpha$ ) and heat conductivity ( $\chi_\alpha$ ) normalized by the Bohm values;  $D_B = \chi_B = cT_e/eB$ . The time history of the ion and electron diffusivities and heat conductivity averaged over  $\psi \in [0.68, 1.0]\psi_X$  is shown in figure 8(a). The transport coefficients first increase exponentially in the linear phase and then saturate in the nonlinear phase due to mode coupling. Figure 8(b) shows the radial variation of the ion and electron diffusivities and heat conductivities averaged over time  $t \in [10, 15]R_0/C_s$  at each radial grid point. The turbulence which is localized at  $\psi \sim \psi_X$  where the gradient in the profile is maximum, in the nonlinear phase spreads from edge to the core due to the nonlinear mode coupling. As there is not much turbulence spreading near the magnetic axis, the central region  $\psi \in [0, 0.1]\psi_X$  has been excluded from the simulation domain.

Figure 9 shows the comparison of the spectrum of electrostatic fluctuations between experiment and simulation that spans from  $\sim 0$  kHz to 50 kHz, plotted on the outer mid-plane side of the flux surface with  $\psi = 0.98\psi_X$ . The experimentally recorded spectrum of electrostatic fluctuations shows a broadband of frequencies from  $\sim 0$  to 50 kHz (red) that matches well with the findings of the gyrokinetic simulations (blue) of ADITYA-U tokamak using GTC. The ion diffusivity near to the LCFS of tokamak predicted from the self-consistent simulations using GTC (see figure 8) gives a value  $\sim 0.2 \text{ m}^2 \text{ s}^{-1}$  which roughly matches the experimental estimate derived from the density profile [62], and further cross-checked with UEDGE code simulations [63]. Due to the diagnostic limitations at the present time, a realistic experimental value of the electron heat conductivity is not available. The reported experimental value of the electron heat conductivity has been estimated by assuming a diffusive transport and using an energy

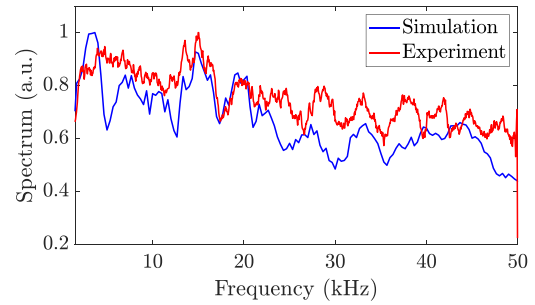


**Figure 9.** The comparison of the spectra of the electrostatic fluctuations from simulation (blue) and experiment (red) near the LCFS.

**Table 3.** Comparison of the transport from the experiment with the simulations near LCFS.

( $\text{m}^2 \text{ s}^{-1}$ )	Experiment	Simulation
$D_i$	0.2	0.25
$\chi_e$	1.5	1.20

confinement time from power balance as  $\chi_e \sim a^2/4\tau_E$ , where  $a$  is the minor radius (0.25 m) and  $\tau_E$  is the energy confinement time [64]. Experimentally,  $\tau_E$  is obtained by the usual method of dividing the stored energy by the input power, that gives  $\tau_E \sim 10$  ms [62]. This estimate of the electron heat conductivity obtained from the experiment is  $\chi_e \sim 1.5 \text{ m}^2 \text{ s}^{-1}$ , which is within 20% of the value  $\chi_e \sim 1.2 \text{ m}^2 \text{ s}^{-1}$  obtained from the simulations (see figure 8). However, it should be pointed out that the experimental estimate is based on the global power balance relation that assumes an average effective transport coefficient  $\chi_e$  that can be significantly different from the local transport coefficient  $\chi_e(\psi \sim \psi_X)$  used in our calculation based on the simulations. Hence the rough agreement between the two values needs to be viewed keeping that context in mind. Table 3 shows the comparison of the transport between the experiment and simulation near to the LCFS.

All these findings illustrate that TEM driven microturbulence is one of the dominant channels for driving the turbulent transport in the ADITYA-U tokamak. These results may be important in setting up future ADITYA-U experiments.

## 5. Conclusion and discussion








To summarize, in this work, global gyrokinetic simulations of the electrostatic microturbulence in the ADITYA-U tokamak for shot # 33536 are carried out in the presence of collisions, using GTC. The linear eigenmode structure is dominated by a trapped electron driven instability, propagating in the electron diamagnetic direction with a real frequency of  $\sim 2.79C_s/R_0$ , and the growth rate of  $\sim 2.98C_s/R_0$ , that lies on the low wavenumber side with  $k_\perp \rho_i \sim 0.7$ . The simulations with and without collisions show that the collisional effects suppress the turbulence and transport to a certain extent. The nonlinear simulations of the microturbulence predict a local ion diffusivity value that is close to the experimentally reported value of  $\sim 0.2 \text{ m}^2 \text{ s}^{-1}$ . The electron heat conductivity estimated from the experimentally measured energy confinement time is also within 20% of the simulated value of  $\sim 1.2 \text{ m}^2 \text{ s}^{-1}$ . However, as discussed before, the near agreement between these transport rates has to be viewed in the context of the assumptions underlying the two estimates. It should be kept in mind that the experimental estimate is based on the global power balance relation that assumes an average effective transport coefficient  $\chi_e$  that can be significantly different from the local transport coefficient  $\chi_e(\psi \sim \psi_X)$  used in our calculation based on the simulations. The comparison can be further refined and made more realistic in the future with the availability of better diagnostic measurements on ADITYA-U. The spectrum of electrostatic fluctuations shows a broadband of frequencies from  $\sim 0$  to 50 kHz which agrees with the spectrum obtained from the experiment. The nonlinear simulations show that the zonal flow is not playing an important role in the turbulence saturation, while the nonlinear saturation is dominated by the inverse cascade of the high poloidal and toroidal modes to the lower one. Thus, the electrostatic microturbulence driven by the trapped electrons in the presence of collisions acts as one of the dominant channels for driving the anomalous turbulent transport in the ADITYA-U tokamak. The current work is the first step towards understanding the turbulence and transport in ADITYA-U. From the experimental perspective, the insights gained from this electrostatic microturbulence study may be useful in setting up future ADITYA-U experiments. In the future, we plan to study the impurity transport by the electrostatic microturbulence, effects of equilibrium radial electric fields, and electromagnetic effects in ADITYA-U.

## Acknowledgments

T.S. would like to thank J.H. Nicolau for the helpful discussion. The authors remain grateful to the ADITYA-U operation and diagnostic team for providing the data. This work is supported by National Supercomputing Mission (NSM) (Ref. No.: DST/NSM/R&D\_HPC\_Applications/2021/4), Board of Research in Nuclear Sciences (BRNS Sanctioned No. 39/14/05/2018-BRNS), Science and Engineering Research Board EMEQ program (SERB sanctioned No. EEQ/2017/000164) and Infosys Young Investigator award and US DOE SciDAC ISEP Center. A.S. is thankful to the

Indian National Science Academy (INSA) for their support under the INSA Senior Scientist Fellowship scheme. The results presented in this work have been simulated on ANTYA cluster at Institute of Plasma Research, Gujarat, India, and SahasraT, Param Pravega supercomputers at Indian Institute of Science, Bangalore, India.

## ORCID iDs

Tajinder Singh  <https://orcid.org/0000-0003-0860-3626>  
 Tanmay Macwan  <https://orcid.org/0000-0002-9767-0830>  
 Sarveshwar Sharma  <https://orcid.org/0000-0002-0642-0247>  
 Joydeep Ghosh  <https://orcid.org/0000-0002-4369-1900>  
 Abhijit Sen  <https://orcid.org/0000-0001-9878-4330>  
 Zhihong Lin  <https://orcid.org/0000-0003-2007-8983>  
 Animesh Kuley  <https://orcid.org/0000-0003-2325-6597>

## References

- [1] Ongena J., Koch R., Wolf R. and Zohm H. 2016 Magnetic-confinement fusion *Nat. Phys.* **12** 398–410
- [2] Wesson J. and Campbell D.J. 2018 *Tokamaks* (Oxford: Oxford University Press)
- [3] Wootton A.J., Carreras B.A., Matsumoto H., McGuire K., Peebles W.A., Ritz C.P., Terry P.W. and Zweben S.J. 1990 Fluctuations and anomalous transport in tokamaks *Phys. Fluids B* **2** 2879–903
- [4] Horton W. 1999 Drift waves and transport *Rev. Mod. Phys.* **71** 735–78
- [5] Bigot B. 2019 Progress toward ITER's first plasma *Nucl. Fusion* **59** 112001
- [6] Doyle E.J. et al 2007 Progress in the ITER physics basis chapter 2: plasma confinement and transport *Nucl. Fusion* **47** S18
- [7] Candy J. and Waltz R.E. 2003 Anomalous transport scaling in the DIII-D tokamak matched by supercomputer simulation *Phys. Rev. Lett.* **91** 045001
- [8] Lin Z., Ethier S., Hahn T.S. and Tang W.M. 2002 Size scaling of turbulent transport in magnetically confined plasmas *Phys. Rev. Lett.* **88** 195004
- [9] Tang W.M. 2008 Scientific and computational challenges of the fusion simulation project (FSP) *J. Phys.: Conf. Ser.* **125** 012047
- [10] Garbet X., Idomura Y., Villard L. and Watanabe T.H. 2010 Gyrokinetic simulations of turbulent transport *Nucl. Fusion* **50** 043002
- [11] Lin Z., Hahn T.S., Lee W.W., Tang W.M. and White R.B. 1998 Turbulent transport reduction by zonal flows: massively parallel simulations *Science* **281** 1835–7
- [12] Jolliet S., Bottino A., Angelino P., Hatzky R., Tran T.M., Mcmillan B.F., Sauter O., Appert K., Idomura Y. and Villard L. 2007 A global collisionless PIC code in magnetic coordinates *Comput. Phys. Commun.* **177** 409–25
- [13] Lang J., Parker S.E. and Chen Y. 2008 Nonlinear saturation of collisionless trapped electron mode turbulence: zonal flows and zonal density *Phys. Plasmas* **15** 055907
- [14] Parker S.E. and Lee W.W. 1993 A fully nonlinear characteristic method for gyrokinetic simulation *Phys. Fluids B* **5** 77–86
- [15] Jenko F., Dorland W., Kotschenreuther M. and Rogers B.N. 2000 Electron temperature gradient driven turbulence *Phys. Plasmas* **7** 1904–10
- [16] Watanabe T.-H. and Sugama H. 2005 Velocity–space structures of distribution function in toroidal ion temperature gradient turbulence *Nucl. Fusion* **46** 24–32

- [17] Candy J. and Waltz R.E. 2003 An Eulerian gyrokinetic-Maxwell solver *J. Comput. Phys.* **186** 545–81
- [18] Grandgirard V. *et al* 2007 Global full-*f* gyrokinetic simulations of plasma turbulence *Plasma Phys. Control. Fusion* **49** B173–82
- [19] Ross D.W. and Dorland W. 2002 Comparing simulation of plasma turbulence with experiment. II. Gyrokinetic simulations *Phys. Plasmas* **9** 5031–5
- [20] White A.E. *et al* 2008 Measurements of core electron temperature and density fluctuations in DIII-D and comparison to nonlinear gyrokinetic simulations *Phys. Plasmas* **15** 056116
- [21] Howard N.T., White A.E., Reinke M.L., Greenwald M., Holland C., Candy J. and Walk J.R. 2013 Validation of the gyrokinetic model in ITG and TEM dominated L-mode plasmas *Nucl. Fusion* **53** 123011
- [22] Diamond P.H., Itoh S.-I., Itoh K. and Hahm T.S. 2005 Zonal flows in plasma—a review *Plasma Phys. Control. Fusion* **47** R35
- [23] Ernst D.R., Lang J., Nevins W.M., Hoffman M., Chen Y., Dorland W. and Parker S. 2009 Role of zonal flows in trapped electron mode turbulence through nonlinear gyrokinetic particle and continuum simulation *Phys. Plasmas* **16** 055906
- [24] Xiao Y., Holod I., Zhang W., Klasky S. and Lin Z. 2010 Fluctuation characteristics and transport properties of collisionless trapped electron mode turbulence *Phys. Plasmas* **17** 022302
- [25] Dannert T. and Jenko F. 2005 Gyrokinetic simulation of collisionless trapped-electron mode turbulence *Phys. Plasmas* **12** 072309
- [26] Lang J., Chen Y. and Parker S.E. 2007 Gyrokinetic  $\delta f$  particle simulation of trapped electron mode driven turbulence *Phys. Plasmas* **14** 082315
- [27] Ajay C.J., Brunner S. and Ball J. 2021 Effect of collisions on non-adiabatic electron dynamics in ITG-driven microturbulence *Phys. Plasmas* **28** 092303
- [28] Ryter F., Angioni C., Peeters A.G., Leuterer F., Fahrbach H.-U. and Suttrop W. 2005 Experimental study of trapped-electron-mode properties in tokamaks: threshold and stabilization by collisions *Phys. Rev. Lett.* **95** 085001
- [29] Hu W., Feng H.-Y. and Dong C. 2018 Collisional effects on drift wave microturbulence in tokamak plasmas *Chin. Phys. Lett.* **35** 105201
- [30] Lau C.K., Fulton D.P., Holod I., Lin Z., Binderbauer M., Tajima T. and Schmitz L. 2017 Drift-wave stability in the field-reversed configuration *Phys. Plasmas* **24** 082512
- [31] Wang H.Y., Holod I., Lin Z., Bao J., Fu J.Y., Liu P.F., Nicolau J.H., Spong D. and Xiao Y. 2020 Global gyrokinetic particle simulations of microturbulence in W7-X and LHD stellarators *Phys. Plasmas* **27** 082305
- [32] Nicolau J.H., Choi G., Fu J., Liu P., Wei X. and Lin Z. 2021 Global gyrokinetic simulation with kinetic electron for collisionless damping of zonal flow in stellarators *Nucl. Fusion* **61** 126041
- [33] Singh T., Nicolau J.H., Lin Z., Sharma S., Sen A. and Kuley A. 2022 Global gyrokinetic simulations of electrostatic microturbulent transport using kinetic electrons in LHD stellarator *Nucl. Fusion* **62** 126006
- [34] Tanna R.L. *et al* 2018 Plasma production and preliminary results from the ADITYA upgrade tokamak *Plasma Sci. Technol.* **20** 074002
- [35] Tanna R.L. *et al* 2017 Overview of recent experimental results from the Aditya tokamak *Nucl. Fusion* **57** 102008
- [36] Tanna R.L. *et al* 2019 Overview of operation and experiments in the ADITYA-U tokamak *Nucl. Fusion* **59** 112006
- [37] Tanna R.L. *et al* 2022 Overview of recent experimental results from the ADITYA-U tokamak *Nucl. Fusion* **62** 042017
- [38] Macwan T. *et al* ADITYA-U Team 2021 Gas-puff induced cold pulse propagation in ADITYA-U tokamak *Nucl. Fusion* **61** 096029
- [39] Scott B. 1997 Three-dimensional computation of drift Alfvén turbulence *Plasma Phys. Control. Fusion* **39** 1635
- [40] Atrey P.K., Pujara D., Mukherjee S. and Tanna R.L. 2019 Design, development and operation of seven channels' 100-GHz interferometer for plasma density measurement *IEEE Trans. Plasma Sci.* **47** 1316–21
- [41] Shukla G. *et al* 2019 Observations of toroidal plasma rotation reversal in the Aditya-U tokamak *Nucl. Fusion* **59** 106049
- [42] Sharma D., Srinivasan R., Ghosh J. and Chattopadhyay P. 2020 Aditya upgradation—equilibrium study *Fusion Eng. Des.* **160** 111933
- [43] Liewer P.C., McChesney J.M., Zweben S.J. and Gould R.W. 1986 Temperature fluctuations and heat transport in the edge regions of a tokamak *Phys. Fluids* **29** 309–17
- [44] Nold B., Ribeiro T.T., Ramisch M., Huang Z., Müller H.W., Scott B.D. and Stroth U. (The ASDEX Upgrade Team) 2012 Influence of temperature fluctuations on plasma turbulence investigations with Langmuir probes *New J. Phys.* **14** 063022
- [45] Dubin D.H.E., Krommes J.A., Oberman C. and Lee W.W. 1983 Nonlinear gyrokinetic equations *Phys. Fluids* **26** 3524–35
- [46] Lee W.W. 1987 Gyrokinetic particle simulation model *J. Comput. Phys.* **72** 243–69
- [47] Brizard A.J. and Hahm T.S. 2007 Foundations of nonlinear gyrokinetic theory *Rev. Mod. Phys.* **79** 421–68
- [48] Lin Z., Tang W.M. and Lee W.W. 1995 Gyrokinetic particle simulation of neoclassical transport *Phys. Plasmas* **2** 2975–88
- [49] Lin Z., Nishimura Y., Xiao Y., Holod I., Zhang W.L. and Chen L. 2007 Global gyrokinetic particle simulations with kinetic electrons *Plasma Phys. Control. Fusion* **49** B163–72
- [50] Xiao Y., Holod I., Wang Z., Lin Z. and Zhang T. 2015 Gyrokinetic particle simulation of microturbulence for general magnetic geometry and experimental profiles *Phys. Plasmas* **22** 022516
- [51] Falgout R.D., Jones J.E. and Yang U.M. 2006 The design and implementation of hypre, a library of parallel high performance preconditioners. *Numerical Solution of Partial Differential Equations on Parallel Computers* 51 ed A.M. Bruaset and A. Tveito (Berlin: Springer-Verlag) pp 267–94
- [52] Fulton D.P., Lin Z., Holod I. and Xiao Y. 2014 Microturbulence in DIII-D tokamak pedestal. I. Electrostatic Instabilities *Phys. Plasmas* **21** 042110
- [53] Duff J.R., Williams Z.R., Brower D.L., Chapman B.E., Ding W.X., Pueschel M.J., Sarff J.S. and Terry P.W. 2018 Observation of trapped-electron-mode microturbulence in reversed field pinch plasmas *Phys. Plasmas* **25** 010701
- [54] Ernst D.R. *et al* (Alcator C-Mod Group) 2004 Role of trapped electron mode turbulence in internal transport barrier control in the Alcator C-Mod Tokamak *Phys. Plasmas* **11** 2637–48
- [55] Arnichand H. *et al* 2015 Identification of trapped electron modes in frequency fluctuation spectra *Plasma Phys. Control. Fusion* **58** 014037
- [56] Hoang G.T., Bourdelle C., Garbet X., Giruzzi G., Aniel T., Ottaviani M., Horton W., Zhu P. and Budny R.V. 2001 Experimental determination of critical threshold in electron transport on Tore Supra *Phys. Rev. Lett.* **87** 125001
- [57] Hillesheim J.C. *et al* 2013 Observation of a critical gradient threshold for electron temperature fluctuations in the DIII-D tokamak *Phys. Rev. Lett.* **110** 045003
- [58] Villegas D., Guirlet R., Bourdelle C., Hoang G.T., Garbet X. and Sabot R. 2010 Experimental electron temperature

- gradient dependence of heavy impurity transport in fusion devices *Phys. Rev. Lett.* **105** 035002
- [59] Zhong W.L., Zou X.L., Bourdelle C., Song S.D., Artaud J.F., Aniel T. and Duan X.R. 2013 Convective velocity reversal caused by turbulence transition in tokamak plasma *Phys. Rev. Lett.* **111** 265001
- [60] Faber B.J., Pueschel M.J., Proll J.H.E., Xanthopoulos P., Terry P.W., Hegna C.C., Weir G.M., Likin K.M. and Talmadge J.N. 2015 Gyrokinetic studies of trapped electron mode turbulence in the helically symmetric experiment stellarator *Phys. Plasmas* **22** 072305
- [61] Deng C.B., Brower D.L., Anderson D.T., Anderson F.S.B., Briesemeister A. and Likin K.M. 2015 Core density turbulence in the HSX stellarator *Nucl. Fusion* **55** 123003
- [62] Macwan T. 2022 Effect of short gas-puff pulses and biased-electrode on transport, MHD instabilities, plasma-wall interaction and runaway electrons in ADITYA-U tokamak *PhD Thesis* Homi Bhabha National Institute
- [63] Dey R. *et al* 2021 Simulations of edge plasma parameters of ADITYA-U tokamak using UEDGE code (private communication)
- [64] Callen J.D. and Jahns G.L. 1977 Experimental measurement of electron heat diffusivity in a tokamak *Phys. Rev. Lett.* **38** 491–4